SIAM J. APPL. MATH.
Vol. 74, No. 5, pp. 1338–1353

DIMENSIONAL REDUCTION OF A MULTISCALE CONTINUUM MODEL OF MICROTUBULE GLIDING ASSAYS*

CHRISTEL HOHENEGGER†, STEVE COOK‡, AND TAMAR SHINAR§

Abstract. Microtubule gliding assays, in which molecular motors anchored to a plate drive the gliding motion of filaments in a quasi–two-dimensional fluid layer, have been shown to organize into a variety of large-scale patterns. We derive a fully three-dimensional multiscale coarse-grained model of a gliding assay including the evolution of densities of rigid filaments, bound motors, and free motors, coupled to fluid equations. Our model combines continuum theories of polymeric liquids with the force spreading approach of the immersed boundary method. We use dimensional and asymptotic analysis to derive a reduced two-dimensional model and show that, to leading order, the filaments evolve in a plane, similar to what is experimentally observed. We simulate our model numerically with a GPU-based implementation and observe the same qualitative behavior as in experimental work.

Key words. asymptotic analysis, dimensional analysis, Hele-Shaw, microtubule assays, multiscale simulation, active fluids

AMS subject classifications. 76Z99, 76A15, 92C35, 65Z05, 34E10

DOI. 10.1137/140961535

1. Introduction.

Active gels form the basic structural network of the cell and can be synthesized by mixing cytoskeletal filaments and small motor proteins. In such mixtures, the collective behavior is driven by the microscopic ATPase-generated motion of the motor proteins along the filaments. A molecular motor typically consists of a tail, a flexible stalk, and a head with two binding sites. Through the hydrolysis of ATP at the binding sites, the motor grabs, pulls, and releases the filament, yielding a processive directional motion and generating forces inside the cell. Molecular motors have been the subject of many experimental [10, 8, 13, 14, 12, 5] and theoretical [26, 20, 18] studies, which have resulted in a broader understanding of the molecular stepping mechanism and the collaboration of many motors when carrying cargo along filamentous tracks. On a larger scale, mixtures of cytoskeletal filaments and small motor proteins have been shown to self-organize into a variety of macroscopic patterns from asters to vortices to swarms [31, 30, 38]. We study gliding assays, where single motors are adsorbed onto a substrate and filaments, stabilized so that their lengths are fixed, glide over them in a quasi–two-dimensional fluid layer (Figure 1). This reduced system, where filaments do not crosslink, is used to study gliding velocities of microtubules and motor directionality [33] and has been observed to form large-scale patterns [38].

*Received by the editors March 19, 2014; accepted for publication (in revised form) May 27, 2014; published electronically September 9, 2014. The second and third authors were supported by the National Institute of General Medical Sciences of the National Institutes of Health under award R01GM104976. The content is solely the responsibility of the authors and does not necessarily represent the official views of the National Institutes of Health.

http://www.siam.org/journals/siap/74-5/96153.html

†Corresponding author. Department of Mathematics, University of Utah, Salt Lake City, UT 84112 (choheneg@math.utah.edu).

‡Department of Computer Science & Engineering, University of California, Riverside, CA 92521 (scook005@cs.ucr.edu).

§Corresponding author. Department of Computer Science & Engineering, University of California, Riverside, CA 92521 (shinar@cs.ucr.edu).

Systems of fluids, filaments, and motors are inherently multiscale in space and time, making them a challenge to accurately model. Moreover, [41] showed that the macroscopic behavior of these active mixtures is sensitive to the microscopic model. A variety of theoretical models attempt to bridge the understanding of the microscopic mechanisms with the emergent macroscopic phenomena. One computationally intensive approach is to model collections of explicitly represented filaments and motors without coarse-graining [28, 30, 29]. In contrast, other modeling standpoints rely on a generic hydrodynamic theory that is inherently macroscopic [24, 37, 22, 23, 11]. Considering gliding assays specifically, [21, 17] developed a Langevin dynamics model coupling the dynamics of the filament, the dynamics of the motor head, and the elasticity of the motor stalks. Other approaches have exhibited pattern formation through phenomenological particle-based steric interactions [38, 39], while [11] demonstrated the importance of hydrodynamic effects in the collective behavior of large-scale systems of filaments. A final set of approaches starts with a simplified microscopic model and coarse-grains the system via a priori closure approximations to attain a macroscopic description [41, 25]. We take such an approach while additionally considering fluctuations in motor and filament densities, the background flow, and the interactions of the immersed structure and the fluid. This allows us to directly incorporate knowledge of the microscale mechanisms while maintaining the efficiency of coarse-grained approaches over particle-based approaches in simulating hydrodynamic interactions.

As a first step toward a multiscale model of gliding assays, we develop a three-dimensional model, including hydrodynamics effects via the coupling of the filaments and the fluid, but we assume a dilute suspension of filaments, thus neglecting steric effects. In contrast to previous modeling approaches, we do not assume that the filaments move in a two-dimensional plane, but instead we show that this results from an asymptotic analysis and Hele-Shaw reduction of the fluid-coupled continuum model. Furthermore, our modeling approach couples the microscale modeling of the attachment and detachment of molecular motors to the mesoscale motion of the filaments, and finally to the macroscale fluid motion. This explicit coupling is obtained by combining continuum theories of polymeric liquids [3] with the force spreading approach of the immersed boundary method [32]. There are three components of our continuum model: a filament conservation equation, conservation equations for bound and free motors, and fluid equations. These coupled equations evolve on three length scales: L, the length of the side of the cover slip; l, the length of the filament; and L_m, the length of the motor stalk. We assume that $L_m \ll H = \varepsilon L \ll L$, where H is the distance between the cover slip and the plate.

The remainder of the paper is organized as follows. In section 2, we derive the full three-dimensional continuum model focusing on the fluid coupling. Next, in section 3, we nondimensionalize the model and neglect small terms. In section 4, we obtain reduced two-dimensional gap-averaged equations through an asymptotic analysis and depth averaging, and we show that in this reduced formulation the filaments move in a two-dimensional plane parallel to the bottom plate. Section 5 is devoted to the numerical implementation, which is spectral for the fluid equations and second order in time and space for the evolution equations. Difficulties resulting from the high dimensionality are resolved by exploiting data sparsity and using GPU parallelism. Finally, section 6 illustrates the reduced model and numerical implementation for a set of parameters chosen to be experimentally relevant. In this case, our simulation shows the emergence of ordered subregions of filaments and motors as observed experimentally. We end with a short conclusion in section 7.

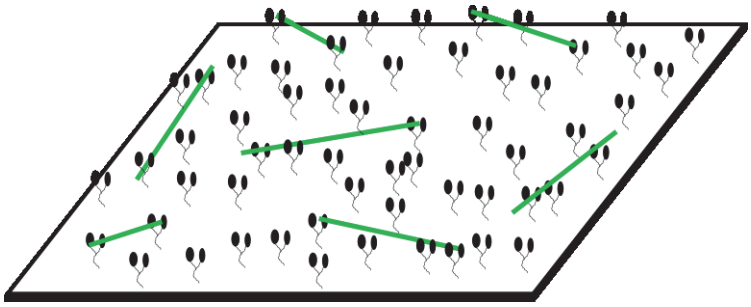

FIG. 1. *Microtubule gliding assay setup. Motor protein (black) tails are anchored to a fixed plate, while their heads bind and pull microtubule filaments (green lines, online) suspended in a liquid.*

2. Model. In a gliding assay, motor protein tails are anchored to a horizontal plate, while their heads are free to bind and pull filaments suspended in a liquid. Figure 1 illustrates the experimental setup. Since there are no free motor complexes in suspension and a motor can only attach to a single filament, there is no crosslinking of filaments via motor complexes.

In Table 1, we summarize the physical parameters relevant for the gliding assay geometry, based on values reported in the literature.

TABLE 1

List of relevant physical parameters and their values as reported in the literature. (sp) denotes simulation parameters used in the referenced source.

Parameter	Symbol	Value or Range	Source
Motor attachment rate	k_{on}	.005–.05s^{-1} (sp)	[37]
		.04–50s^{-1} (sp)	[28]
		50s^{-1}	[40]
Motor detachment rate	k_{off}	.083–.167s^{-1}	[15]
		.005–.05s^{-1} (sp)	[37]
		.04–50s^{-1} (sp)	[28]
		.5s^{-1}	[40]
Motor maximum speed	$V_{\max}$	500–750nm/s	[15]
		1μm/s (sp)	[28, 17, 37]
Motor stall force	F_{stall}	0.5–2pN	[28]
		5pN	[17]
Motor length (fully stretched)	L_m	50nm	[17]
Motor capture radius	r_{c}	10–22nm	[17]
Chamber length	L	5–18mm	[15]
		3–15mm	[27]
Chamber height	H	110μm	[15]
		100μm	[27]
Filament length	l	.7–7μm	[15]
		50μm	[16]
		1μm	[17]
Fluid viscosity	μ	0.5pNs/μm^2	[17]
Fluid velocity	U	10μm/s	[39]

2.1. Filament conservation equation. For a dilute suspension of filaments, we denote by $\Psi(\mathbf{x}, \mathbf{p}, t)$ the three-dimensional probability density function of the filament center-of-mass position $\mathbf{x}$ and orientation $\mathbf{p}$ with $|\mathbf{p}| = 1$. Here, we parametrize a *rigid, fixed length* filament by $\mathbf{x} + s\mathbf{p}$, where $s \in [-l, l]$ is the arc length parameter and we neglect bending, growth, or shrinkage of filaments. The total number of filaments $N = \iint \Psi(\mathbf{x}, \mathbf{p}, t) d\mathbf{x} d\mathbf{p}$ is conserved, and the Smoluchowski equation or the conservation of mass in probability for Ψ is [2, 1, 6]

$$\partial_t \Psi + \nabla_x \cdot (\dot{\mathbf{x}}\Psi) + \nabla_p \cdot (\dot{\mathbf{p}}\Psi) = 0. \tag{2.1a}$$

To close (2.1a), we use equations for the $\mathbf{x}, \mathbf{p}$ dynamics derived from slender-body theory as in [34, 35] for active swimmers:

$$\dot{\mathbf{x}}_2 = \mathbf{u}_2(\mathbf{x}) - D_{\mathrm{t},||} \nabla_{x_2} \ln \Psi, \tag{2.1b}$$

$$\dot{z} = w(\mathbf{x}) - D_{\mathrm{t},\perp} \partial_z \ln \Psi, \tag{2.1c}$$

$$\dot{\mathbf{p}} = (\mathbf{I} - \mathbf{pp}) \nabla_x \mathbf{u}(\mathbf{x}) \mathbf{p} - D_{\mathrm{r}} \nabla_p \ln \Psi. \tag{2.1d}$$

Here $\nabla_p = (\mathbf{I} - \mathbf{pp}) \partial_{\mathbf{p}}$ is the gradient on the unit sphere, $\mathbf{u} = (\mathbf{u}_2, w)$ is the fluid velocity, and the subscript 2 denotes the in-plane coordinates x, y. To obtain (2.1b)–(2.1d), we assumed that the background flow $\mathbf{u}$ is linear along the slender and rigid filaments. Thus $\mathbf{u}$ can be written as $\mathbf{u}(\mathbf{x}+s\mathbf{p}) = \mathbf{u}(\mathbf{x}) + s\nabla\mathbf{u}(\mathbf{x})\mathbf{p}$. While in the theory of active swimmers, a swimming velocity appears in (2.1b), in our model the motor force acts directly on the fluid and indirectly on the filaments as they move passively with the fluid. This is similar to the approach taken in the immersed boundary method, which was originally developed for flexible passive fibers and membranes immersed in fluids [32]. In our case, the filaments are rigid, resulting in an additional stress on the fluid due to the filaments' resistance to deformation. We discuss this term in section 2.2. In the present model, we do not include thermal fluctuations; instead we consider generalized diffusive terms intended to phenomenologically model small-scale effects due to the surrounding fluid [35]. $D_{\mathrm{t},||}$, $D_{\mathrm{t},\perp}$, and D_{r} are the in-plane translational, out-of-plane translational, and rotational diffusion coefficients, respectively. Physically, if $D_{\mathrm{t},||} = D_{\mathrm{t},\perp} = D_{\mathrm{r}} = 0$, then (2.1b) says that the center-of-mass passively follows the background velocity $\mathbf{u}(\mathbf{x})$, and (2.1d) says that the rate of change in orientation is given by $\nabla\mathbf{u}(\mathbf{x})\mathbf{p}$. The projection operator $(\mathbf{I} - \mathbf{pp})$ in (2.1d) ensures that the length of the filament is constant, i.e., $|\mathbf{p}| = 1$ or $\mathbf{p} \cdot \dot{\mathbf{p}} = 0$.

2.2. Fluid equations. Using the characteristic numbers given in Table 1 for the fluid velocity and characteristic length yields a small Reynolds number, and hence the convective acceleration is negligible. Furthermore, the frequency parameter given by the time scale of the molecular force is small compared to the Reynolds number, and inertia is negligible. Thus, the fluid equations are the incompressible Stokes equations with extra stress and an external force:

$$-\mu \Delta_x \mathbf{u}(\mathbf{x}, t) + \nabla_x q(\mathbf{x}, t) = \nabla_{\mathbf{x}} \cdot \boldsymbol{\sigma}^{\mathrm{p}}(\mathbf{x}) + \mathbf{f}_{\mathrm{m}}(\mathbf{x}, t), \quad \nabla_x \cdot \mathbf{u} = 0. \tag{2.2}$$

Here, $\mathbf{f}_{\mathrm{m}}$ is the force density due to the motors acting at $\mathbf{x}$ on the immersed filaments, q is the pressure, and $\boldsymbol{\sigma}^{\mathrm{p}}$ is the extra stress arising from the microstructure [2]. For passive filaments, $\boldsymbol{\sigma}^{\mathrm{p}}$ can be decomposed into two contributions: $\boldsymbol{\sigma}^{\mathrm{p}} = \boldsymbol{\sigma}^{\mathrm{p}}_B + \boldsymbol{\sigma}^{\mathrm{p}}_F$ [9]. $\boldsymbol{\sigma}^{\mathrm{p}}_B$ arises from Brownian rotations and is modeled as $\boldsymbol{\sigma}^{\mathrm{p}}_B = 3kT\mathbf{D}$, where $\mathbf{D} = \int \Psi \left(\mathbf{pp} - \mathbf{I}/3\right) d\mathbf{p}$. This term is small relative to the motor-based force [4], and we neglect it. $\boldsymbol{\sigma}^{\mathrm{p}}_F$ represents the resistance of the filaments to deformation and is modeled

as $\boldsymbol{\sigma}_F^{\mathrm{p}} = \sigma_f \mathbf{S} : \mathbf{E}$, where $\mathbf{S} = \int \Psi \left(\mathbf{pppp} - \mathbf{Ipp}/3\right) d\mathbf{p}$, $\mathbf{E} = \left(\nabla_x \mathbf{u} + \nabla_x \mathbf{u}^T\right)/2$ is the rate-of-strain tensor, and $\sigma_f = l^3/(3c)$ is a coefficient depending on the aspect ratio r of the filament ($c = \log(2/r)/(4\pi\mu) > 0$). The boundary conditions are doubly periodic in x, y and no-slip at $z = \pm H/2$.

2.3. Bound and free motor equations. A motor that walks in a direction $\mathbf{p}$ under a load $\mathbf{F}$ will step with a speed V given by the single motor load-velocity relationship [13]. Here, the load on the motor is the force exerted on the motor head due to the motor's intrinsic motion. Since we do not model that length scale directly, we make the simplifying assumption that the motor is subject to a load of one-half of its stall force and walks at one-half of its maximum velocity, giving the simplified equation $\mathbf{F} = -F_{\mathrm{st}}\mathbf{p}/2$. The motor force $\mathbf{F}$ gives the force magnitude and direction generated by a motor with tail at $\mathbf{r}_0$ and head on the filament at $\mathbf{r}_1 = \mathbf{y} + s\mathbf{p}$. The motor-based force density at a spatial point $\mathbf{x}$ is then

$$\mathbf{f}_{\mathrm{m}}(\mathbf{x}, t) = -\frac{F_{\mathrm{st}}}{2} \iiiint \mathbf{p}\delta(\mathbf{y} + s\mathbf{p} - \mathbf{x})\Psi(\mathbf{y}, \mathbf{p}, t)\mathcal{M}_{\mathrm{b}}(s, \mathbf{r}_0|\mathbf{y}, \mathbf{p}) ds\, d\mathbf{r}_0\, d\mathbf{y}\, d\mathbf{p}. \tag{2.3}$$

The convolution with the δ-Dirac function converts from the center-of-mass–based description of Ψ to the spatial description of the force density. Here, $\mathcal{M}_{\mathrm{b}}(s, \mathbf{r}_0|\mathbf{x}, \mathbf{p}; t)$ is the *conditional* probability density of bound motors with tail $\mathbf{r}_0$ on the plate and head at s on the given filament $\mathbf{x}, \mathbf{p}$. The total number of bound motors is given by $N_{\mathrm{b}} = \iiiint \mathcal{M}_{\mathrm{b}}\Psi ds\, d\mathbf{r}_0\, d\mathbf{x}\, d\mathbf{p}$. We also introduce $\mathcal{M}_{\mathrm{f}}(\mathbf{r}_0, t)$, the density function of motors with tail at $\mathbf{r}_0$ and free head. The total number of free motors is $N_{\mathrm{f}} = \int \mathcal{M}_{\mathrm{f}} d\mathbf{r}_0$. In the entire system, the total number of motors $N_{\mathrm{m}} = N_{\mathrm{f}} + N_{\mathrm{b}}$ is conserved.

In general, the free and bound motor populations evolve according to a reaction-diffusion-advection equation. In a gliding assay, motor tails are fixed to a plate and cannot diffuse or advect with the flow. Hence, we consider only the conversion between the free and bound populations and the advection and procession of the bound motor heads. Further, we assume that if a motor is close enough to the filament, it can bind to the filament with an attachment rate per filament k_{on} and that a head can detach with a detachment rate k_{off}. We derive the evolution equation for $\mathcal{M}_{\mathrm{b}}$ by considering the conservation law for $\mathcal{M}_{\mathrm{b}}\Psi$, which evolves as

$$\begin{aligned} &\partial_t(\mathcal{M}_{\mathrm{b}}\Psi) + \frac{V_{\max}}{2}\partial_s(\mathcal{M}_{\mathrm{b}}\Psi) + \nabla_x \cdot (\dot{\mathbf{x}}\mathcal{M}_{\mathrm{b}}\Psi) + \nabla_p \cdot (\dot{\mathbf{p}}\mathcal{M}_{\mathrm{b}}\Psi) \\ &\quad = \frac{k_{\mathrm{on}}}{2l \iint_{B_{r_{\mathrm{c}}}} \Psi d\mathbf{p} d\mathbf{x}} \mathcal{M}_{\mathrm{f}}\Psi \mathbb{1}_{B_{r_{\mathrm{c}}}} - k_{\mathrm{off}}\mathcal{M}_{\mathrm{b}}\Psi. \end{aligned} \tag{2.4}$$

Here $\mathbb{1}_{B_{r_{\mathrm{c}}}}$ is the characteristic function on the ball $B_{r_{\mathrm{c}}}$ of (capture) radius r_{c} centered at the attachment point $\mathbf{r}_1$. The three advection terms on the left-hand side express the procession of the motor along the filament with speed $V = V_{\max}/2$ and the motion of the motor-filament complex with the background flow. The source term on the right-hand side expresses the attachment of a free motor at s to the filament $\mathbf{x}, \mathbf{p}$, where the factor $2l \iint_{B_{r_{\mathrm{c}}}} \Psi d\mathbf{p} d\mathbf{x}$ measures the approximate available length of filaments in $B_{r_{\mathrm{c}}}$. Since we are not tracking the position of the head $\mathbf{r}_1$, then, for a given filament $\mathbf{x}, \mathbf{p}$, a head attaches at s with uniform probability in $B_{r_{\mathrm{c}}}$. The sink term represents the detachment of a bound motor. Using (2.1a) to eliminate Ψ, (2.4)

becomes

$$\begin{aligned}\partial_t \mathcal{M}_{\rm b} + \frac{V_{\max}}{2}\partial_s \mathcal{M}_{\rm b} + \dot{\mathbf{x}}\cdot\nabla_x \mathcal{M}_{\rm b} + \dot{\mathbf{p}}\cdot\nabla_p \mathcal{M}_{\rm b} \\ = \frac{k_{\rm on}}{2l\iint_{B_{r_{\rm c}}}\Psi d\mathbf{p}d\mathbf{x}}\mathcal{M}_{\rm f}\mathbb{1}_{B_{r_{\rm c}}} - k_{\rm off}\mathcal{M}_{\rm b}.\end{aligned} \tag{2.5a}$$

We impose an additional condition on detachment. In particular, a head detaches if the motor reaches the end of the filament (i.e., $|s| > l$). We also note that a motor should detach if the motor force exceeds a threshold. Since we assume a constant motor force, we do not encounter this case.

Finally, since the total number of motors $N_{\rm m}$ is conserved, we define the free motor density $\mathcal{M}_{\rm f}$ implicitly as

$$\mathcal{M}_{\rm f} = \mathcal{M} - \iiint \mathcal{M}_{\rm b}\, ds\, d\mathbf{x}\, d\mathbf{p}, \tag{2.5b}$$

where $\mathcal{M}$ is the total density of motors with tails at $\mathbf{r}_0$.

3. Nondimensionalized equations. In order to simplify the model described in section 2, we start by nondimensionalizing the equations and determining characteristic scales.

3.1. Fluid equations. We first nondimensionalize the incompressible Stokes equations (2.2). Let the characteristic length be L in the x and y directions and $H = \varepsilon L$ in the z direction ($\varepsilon \ll 1$), let the characteristic velocity be U in the x and y directions and W in the z direction, and let the characteristic fluid time scale be $T = L/U$. Since the flow time scale in the z direction is the same as in the x, y plane, we must have $W = \varepsilon U$. We denote with primes nondimensional quantities. Substituting the corresponding equations, we note that the nondimensional gradient of $\mathbf{u}$ is

$$\nabla_x \mathbf{u} = \frac{U}{L}\begin{pmatrix} \nabla_{x_2'}\mathbf{u}_2' & \frac{1}{\varepsilon}\partial_{z'}\mathbf{u}_2' \\ \varepsilon\nabla_{x_2'}w'^T & \partial_{z'}w' \end{pmatrix} := \frac{1}{T}\nabla_{x'}\mathbf{u}'. \tag{3.1}$$

From (3.1), it follows that the extra stress due to the resistance to deformation $\boldsymbol{\sigma}_F^{\rm p}$ has the form $\sigma_f n/T \approx 10^{-4}$ for the dilute microtubule suspensions considered here, so we neglect it. The pressure and force density are nondimensionalized with characteristic pressure Q and force density F. Denoting the components of the force density by $\mathbf{f}_{\rm m} = (\mathbf{f}_{\rm m,2}, h) = F(\mathbf{f}_{\rm m,2}', h')$ and neglecting the extra stress contributions, the Stokes equations (2.2) become

$$\nabla_{x_2'}\mathbf{u}_2' + \partial_{z'}w' = 0, \tag{3.2a}$$

$$-\Delta_{x_2'}\mathbf{u}_2' - \frac{1}{\varepsilon^2}\partial_{z'z'}\mathbf{u}_2' + \frac{LQ}{\mu U}\nabla_{x_2'}q' = \frac{FL^2}{\mu U}\mathbf{f}_{\rm m,2}', \tag{3.2b}$$

$$-\Delta_{x_2'}w' - \frac{1}{\varepsilon^2}\partial_{z'z'}w' + \frac{LQ}{\varepsilon^2\mu U}\partial_{z'}q' = \frac{FL^2}{\varepsilon\mu U}h'. \tag{3.2c}$$

3.2. Filament equations. We nondimensionalize the filament equation (2.1) with the same scales as the fluid equations, and we nondimensionalize Ψ by the total

concentration of filaments $n = N/(\varepsilon L^3)$, setting $n\Psi'(\mathbf{x}', \mathbf{p}, t') = \Psi(L\mathbf{x}_2', \varepsilon L z, \mathbf{p}, Tt')$. We find

$$\partial_{t'}\Psi' + \nabla_{x'} \cdot (\mathring{\mathbf{x}}'\Psi') + \nabla_p \cdot (\mathring{\mathbf{p}}\Psi') = 0, \tag{3.3a}$$

$$\mathring{\mathbf{x}}_2' = \mathbf{u}_2' - \frac{D_{\mathrm{t},||}T}{L^2}\nabla_{x_2'} \ln \Psi', \quad \mathring{z}' = w' - \frac{D_{\mathrm{t},\perp}T}{\varepsilon^2 L^2}\partial_{z'} \ln \Psi', \tag{3.3b}$$

$$\mathring{\mathbf{p}} = (\mathbf{I} - \mathbf{pp})\nabla_{x'}\mathbf{u}'\mathbf{p} - D_{\mathrm{r}}T\nabla_p \ln \Psi', \tag{3.3c}$$

where $\mathring{\cdot}$ indicates the time derivative with respect to t' and $\nabla_{x'}\mathbf{u}'$ refers to the tensor given explicitly in (3.1).

3.3. Bound and free motor equations. Since the motors evolve on a smaller scale than the fluid, we introduce new characteristic scales. We take the filament half-length l as the length scale for motor evolution. We also define a new time scale, $\tau = l/V_{\max}$. We denote with stars the new nondimensional quantities and keep the prime notation for quantities that depend on both scales. We choose to nondimensionalize the density of bound and free motors to the fraction of bound, $N_{\mathrm{b}}/N_{\mathrm{m}}$, and free $N_{\mathrm{f}}/N_{\mathrm{m}}$ motors, respectively. In other words, we set

$$\mathcal{M}_{\mathrm{b}}(s, \mathbf{r}_0|\mathbf{x}, \mathbf{p}; t) = \frac{N_{\mathrm{m}}}{NL^2 l}\mathcal{M}_{\mathrm{b}}'(ls^*, L\mathbf{r}_0'|L\mathbf{x}_2', \varepsilon L z', \mathbf{p}; \tau t^*),$$
$$\mathcal{M}_{\mathrm{f}}(\mathbf{r}_0, t) = \frac{N_{\mathrm{m}}}{L^2}\mathcal{M}_{\mathrm{f}}'(L\mathbf{r}_0, \tau t^*).$$

Substituting the appropriate definitions into (2.5), the nondimensional evolution equations for $\mathcal{M}_{\mathrm{b}}'$ and $\mathcal{M}_{\mathrm{f}}'$ are

$$\begin{aligned}\partial_{t^*}\mathcal{M}_{\mathrm{b}}' + \frac{1}{2}\partial_{s'}(\mathcal{M}_{\mathrm{b}}') + \frac{\tau}{T}\mathring{\mathbf{x}}' \cdot \nabla_{\mathbf{x}'}\mathcal{M}_{\mathrm{b}}' + \frac{\tau}{T}\mathring{\mathbf{p}} \cdot \nabla_p \mathcal{M}_{\mathrm{b}}' \\ = \frac{k_{\mathrm{on}}'}{\iint_{B_{r_{\mathrm{c}}'}} \Psi' d\mathbf{x}' d\mathbf{p}}\mathcal{M}_{\mathrm{f}}' \mathbb{1}_{B_{r_{\mathrm{c}}'}} - k_{\mathrm{off}}'\mathcal{M}_{\mathrm{b}}',\end{aligned} \tag{3.4a}$$

$$\mathcal{M}_{\mathrm{f}}' = \mathcal{M}' - \iiint \mathcal{M}_{\mathrm{b}}'\Psi' ds'\, d\mathbf{x}'\, d\mathbf{p}, \tag{3.4b}$$

where $k_{\mathrm{on}}' = k_{\mathrm{on}}\tau/2$, $k_{\mathrm{off}}' = k_{\mathrm{off}}\tau$, $B_{r_{\mathrm{c}}'}$ is the nondimensional capture ball, and $\mathcal{M} = N_{\mathrm{m}}/(L^2)\mathcal{M}'$. Finally, nondimensionalizing the force density (2.3) and integrating over y_z, we have

$$\begin{aligned}\mathbf{f}_{\mathrm{m}}(\mathbf{x}, t) &= F\mathbf{f}_{\mathrm{m}}'(L\mathbf{x}_2', \varepsilon L x_z, Tt') \\ &= -\frac{F_{\mathrm{st}}N_{\mathrm{m}}}{2\varepsilon L^3}\iiiint \mathbf{p}\delta\left(\mathbf{y}_2' + \frac{l\sin\phi}{L}s^*\mathbf{p}_2 - \mathbf{x}_2'\right)\Psi'\left(\mathbf{y}_2', x_z' + \frac{l}{\varepsilon L}\cos\phi, \mathbf{p}, t'\right) \\ &\quad \times \mathcal{M}_{\mathrm{b}}\left(s^*, \mathbf{r}_0'|\mathbf{y}_2', x_z' + \frac{l}{\varepsilon L}\cos\phi, \mathbf{p}; t^*\right) ds^* d\mathbf{r}_0' d\mathbf{y}_2' d\mathbf{p},\end{aligned} \tag{3.5}$$

where (ϕ, θ) are the polar and azimuthal angles, respectively, and $\mathbf{p}_2 = (\cos\theta, \sin\theta)$. The above equation yields the characteristic force $F = F_0/\varepsilon$ with $F_0 = F_{\mathrm{st}}N_{\mathrm{m}}/L^3$.

4. Two-dimensional reduction. In this section, we reduce the spatial dimension of our system of equations by performing an asymptotic analysis of the fluid equations in $\varepsilon \ll 1$. For clarity of exposition, in the remainder of the paper we drop the primes and replace the open circles with dots and s^* by s.

4.1. Fluid equations. We reduce the fluid equations following the standard Hele-Shaw approach [19]. For the solution to the leading order equation in (3.2b) to be nontrivial, the pressure term and/or the forcing term has to balance the last viscous term. If the forcing term is not one of the dominating terms, then the fluid equations reduce to those of a Newtonian Hele-Shaw cell and are not driven by the motor forces, in contrast to the gliding assay. Therefore, using the characteristic force derived at the end of section 3, we have

$$\frac{FL^2}{\mu U} = \frac{F_0 L^2}{\varepsilon \mu U} = O\left(\frac{1}{\varepsilon^2}\right).$$

For the above relationship to be asymptotically valid, we have $U = O(\varepsilon)$ and we set $U = \varepsilon U_0$. From the definition of the characteristic time, we have $T = L/U = T_0/\varepsilon$ with $T_0 = L/U_0$.

We now discuss the order of the pressure term. If the pressure term is of lower order than the force term, then there are two cases to consider: $Q = O(1)$ and $Q = O(\varepsilon^m)$ with $m \geq 1$. In the latter case, the only leading order term in the z-momentum equation (3.2c) is the force term, which is therefore unbalanced, making this case impossible. In the first case, the pressure term balances the force term in the z-momentum equation (3.2c). But, since the pressure term drops out of the x, y-momentum equations (3.2b), the continuity equation (3.2a) cannot be satisfied without imposing a condition on the forcing term, so this case is also impossible. Therefore, we have

$$\frac{LQ}{\mu U} = \frac{LQ}{\varepsilon \mu U_0} = O\left(\frac{1}{\varepsilon^2}\right)$$

as well. Consequently, Q scales like $1/\varepsilon$, and we set $Q = Q_0/\varepsilon$. As a result from the previous discussion, the leading order terms in (3.2) are $O(1)$ in (3.2a), $O(1/\varepsilon^2)$ in (3.2b), and $O(1/\varepsilon^4)$ in (3.2c).

Next, we perform the asymptotic analysis and consider the leading order terms in the momentum equations (3.2b). Setting $A_0 = LQ_0/(\mu U_0)$ and $B_0 = F_0 L^2/(\mu U_0)$, we have for the leading $O(1/\varepsilon^2)$ terms

$$-\partial_{zz}\mathbf{u}_2 + A_0 \nabla_2 q = B_0 \mathbf{f}_{\mathrm{m},2}. \tag{4.1}$$

In the z-momentum equation (3.2c), the pressure term is the only leading $O(1/\varepsilon^4)$ term, and (3.2c) reduces to $\partial_z q = 0$, which implies that q is independent of z, in other words, $q(\mathbf{x}_2, z) = q(\mathbf{x}_2)$. Integrating (4.1) twice with respect to z, we find that

$$-\mathbf{u}_2(\mathbf{x}_2, z) + \boldsymbol{\alpha_0} z + \boldsymbol{\alpha_1} = -\frac{A_0}{2} z^2 \nabla_2 q(\mathbf{x}_2) + B_0 \mathbb{I}(z),$$

where $\mathbb{I}(z) = \int_{-1/2}^{z} \int_{-1/2}^{z'} \mathbf{f}_{\mathrm{m},2}(\mathbf{x}_2, z'') dz'' dz'$. Using the no-slip boundary conditions at $z = \pm 1/2$, we obtain the constants of integration

$$\boldsymbol{\alpha}_0 = B_0 \mathbb{I}(1/2) \quad \text{and} \quad \boldsymbol{\alpha}_1 = -\frac{A_0}{8} \nabla_2 q(\mathbf{x}_2) + \frac{B_0}{2} \mathbb{I}(1/2).$$

Because $\varepsilon \ll 1$, we now define a gap-averaged velocity $\bar{\mathbf{u}}_2(\mathbf{x}_2) = \int \mathbf{u}_2(\mathbf{x}_2, z) dz$. Averaging the continuity equation (3.2a) over the gap and using the no-slip boundary conditions yields

$$\nabla_2 \cdot \bar{\mathbf{u}}_2 = 0. \tag{4.2a}$$

Further, substituting the values of the integration constants and integrating, we obtain the gap-averaged two-dimensional velocity field $\bar{\mathbf{u}}_2(\mathbf{x}_2)$ driven by the x, y-component of the force density $\mathbf{f}_{\mathrm{m},2}$:

$$\bar{\mathbf{u}}_2(\mathbf{x}_2) = -\frac{A_0}{12}\nabla_2 q(\mathbf{x}_2) + \frac{B_0}{2}\mathbb{I}\left(\frac{1}{2}\right) - B_0\int \mathbb{I}(z)dz. \tag{4.2b}$$

Equations (4.2) are the gap-averaged two-dimensional forced Stokes equations. These equations are very similar to those obtained for non-Newtonian Hele-Shaw flows [19]. We also remark that the integral operator and its mean can be expressed as moments of the force density by reversing the order of integration:

$$\mathbb{I}(1/2) = \int\left(\frac{1}{2} - z\right)\mathbf{f}_{\mathrm{m},2}(\mathbf{x}_2, z)dz \quad \text{and} \quad \int \mathbb{I}(z)dz = \frac{1}{2}\int\left(\frac{1}{2} - z\right)^2 \mathbf{f}_{\mathrm{m},2}(\mathbf{x}_2, z)dz.$$

4.2. Filament equations. To reduce the evolution equations for the distribution functions Ψ, we again rely on leading order analysis and depth-averaging. Since the diffusion terms represent phenomenologically observed small-scale motions, the diffusion constants are chosen so that these terms are of magnitude comparable to that of the other terms in (3.3b)–(3.3c). Integrating (3.3a) over the gap yields

$$\partial_t\left(\int \Psi dz\right) + \nabla_{x,2}\cdot\left(\int \dot{\mathbf{x}}_2\Psi dz\right) + (\dot{z}\Psi)\Big|_{-1/2}^{1/2} + \nabla_p\cdot\left(\int \dot{\mathbf{p}}\Psi dz\right) = 0. \tag{4.3}$$

In order to express the previous equation in terms of the gap-averaged distribution of filaments $\bar{\Psi}$, we will make use of the general closure approximation $\int f(z)\Psi dz = \bar{f}\bar{\Psi}$ for any function $f(z)$. For a velocity field $\mathbf{u}$ that is approximately parabolic in z, the accuracy of this approximation will depend on the maximum value of ψ_{zz} in the gap. This approximation may degrade if all the filaments are bound, as all the filaments will then be within an $\sim$50nm band relative to the $\sim 100\mu$m gap. However, this is not the case in general. With this closure approximation and the no-slip boundary conditions, (4.3) becomes

$$\partial_t\bar{\Psi} + \nabla_{x,2}\cdot\left(\dot{\bar{\mathbf{x}}}_2\bar{\Psi}\right) + \nabla_p\cdot\left(\int \dot{\mathbf{p}}\Psi dz\right) = 0 \quad \text{with} \quad \dot{\bar{\mathbf{x}}}_2 = \bar{\mathbf{u}}_2 - \frac{D^0_{\mathrm{t},||}T_0}{L^2}\nabla_{x,2}\ln\bar{\Psi}, \tag{4.4}$$

where $D_{\mathrm{t},||} = D^0_{\mathrm{t},||}\varepsilon$. Next, we reduce the rotational flux to two dimensions. To do so, we denote the unit vectors in spherical coordinates by $\hat{\boldsymbol{\phi}}$ and $\hat{\boldsymbol{\theta}}$. Then, expressing $\dot{\mathbf{p}}$ in spherical coordinates as $\dot{\mathbf{p}} = \dot{\phi}\hat{\boldsymbol{\phi}} + \sin\phi\dot{\theta}\hat{\boldsymbol{\theta}}$, taking the dot product of (3.3c) with $\hat{\boldsymbol{\theta}}$ and $\hat{\boldsymbol{\phi}}$, and defining $D_{\mathrm{r}} = D^0_{\mathrm{r}}\varepsilon$, we arrive at

$$\dot{\theta}\sin\phi = \hat{\boldsymbol{\theta}}^T\nabla_x\mathbf{u}\mathbf{p} - \frac{D^0_{\mathrm{r}}T_0}{\sin\phi}\partial_\theta\ln\Psi \quad \text{and} \quad \dot{\phi} = \hat{\boldsymbol{\phi}}^T\nabla_x\mathbf{u}\mathbf{p} - D^0_{\mathrm{r}}T_0\partial_\phi\ln\Psi. \tag{4.5}$$

Recalling the form of $\nabla_x\mathbf{u}$ in (3.1), we let $\mathbf{p} = (\sin\phi\mathbf{p}_2, \cos\phi)$, $\hat{\boldsymbol{\theta}} = (\mathbf{p}_2^\perp, 0)$, and $\hat{\boldsymbol{\phi}} = (\cos\phi\mathbf{p}_2, -\sin\phi)$ with $\mathbf{p}_2^\perp = (-\sin\theta, \cos\theta)$. The leading order term in (4.5) is of order $1/\varepsilon$, and carrying out the matrix multiplications, we obtain

$$\cos\phi\left(\mathbf{p}_2^{\perp T}\partial_z\mathbf{u}_2\right) = 0 \quad \text{and} \quad \cos^2\phi\left(\mathbf{p}_2^T\partial_z\mathbf{u}_2\right) = 0.$$

The only nontrivial solution to the previous equations is $\cos\phi = 0$, that is, $\phi = \frac{\pi}{2}$. In other words, to leading order the filaments lie in a horizontal plane, which has been observed experimentally [38]. In this case, $\nabla_p \cdot (\int \dot{\mathbf{p}}\Psi) = \partial_\theta(\int \dot{\theta}\Psi)$ and $\dot{\theta} = \mathbf{p}_2^{\perp T}\nabla_{x,2}\mathbf{u}_2\mathbf{p}_2 - D_{\mathrm{r}}^0 T_0 \partial_\theta \ln\Psi$, which allows us to reduce the last term in (4.4) to a single θ derivative. Combining everything and applying the closure approximation on the velocity gradient tensor, we arrive at the two-dimensional gap-averaged filament evolution equation

$$\partial_t\bar{\Psi} + \nabla_{x,2}\cdot(\dot{\bar{\mathbf{x}}}_2\bar{\Psi}) + \partial_\theta(\dot{\bar{\theta}}\bar{\Psi}) = 0, \tag{4.6a}$$

$$\dot{\bar{\mathbf{x}}}_2 = \bar{\mathbf{u}}_2 - \frac{D_{\mathrm{t},||}^0 T_0}{L^2}\nabla_2 \ln\bar{\Psi}, \quad \dot{\bar{\theta}} = \mathbf{p}_2^{\perp T}\nabla_{x,2}\bar{\mathbf{u}}_2\mathbf{p}_2 - D_{\mathrm{r}}^0 T_0\partial_\theta \ln\bar{\Psi}. \tag{4.6b}$$

4.3. Bound and free motor equations. Since $T = T_0/\varepsilon$, the last two advective terms on the left of (3.4a) scale like ε and can be neglected. Further, because no other term in (3.4a) depends on ε, the $O(1)$ leading order equation for $\mathcal{M}_{\mathrm{b}}$ is

$$\partial_{t^*}\mathcal{M}_{\mathrm{b}} + \frac{1}{2}\partial_s\mathcal{M}_{\mathrm{b}} = \frac{k_{\mathrm{on}}}{\iint_{B_{r_{\mathrm{c}}}}\Psi d\mathbf{x}d\theta}\mathcal{M}_{\mathrm{f}}\mathbb{1}_{B_{r_{\mathrm{c}}}} - k_{\mathrm{off}}\mathcal{M}_{\mathrm{b}}. \tag{4.7}$$

Integrating over z and using the closure approximation, we obtain the gap-averaged equation for the density of bound and free motors

$$\partial_{t^*}\bar{\mathcal{M}}_{\mathrm{b}} + \frac{1}{2}\partial_s(\bar{\mathcal{M}}_{\mathrm{b}}) = \frac{k_{\mathrm{on}}}{\iint_B \bar{\Psi}d\mathbf{x}_2 d\theta}\mathcal{M}_{\mathrm{f}}\mathbb{1}_B - k_{\mathrm{off}}\bar{\mathcal{M}}_{\mathrm{b}}, \tag{4.8a}$$

$$\mathcal{M}_{\mathrm{f}} = \mathcal{M} - \iiint \bar{\mathcal{M}}_{\mathrm{b}}\bar{\Psi}ds\, d\mathbf{x}_2\, d\theta. \tag{4.8b}$$

Here B is the two-dimensional projection of $B_{r_{\mathrm{c}}}$.

Next, we reduce the motor force density (3.5). Integrating over z, using the closure approximation and $\phi = \pi/2$, we obtain the gap-averaged force density

$$\bar{\mathbf{f}}_m(\mathbf{x}_2,t) = -\frac{1}{2}\iiiint \mathbf{p}_2\delta\left(\mathbf{y}_2 + \frac{l}{L}s\mathbf{p}_2 - \mathbf{x}_2\right)\bar{\Psi}(\mathbf{y}_2,\theta,t)\bar{\mathcal{M}}_b(s,\mathbf{r}_0|\mathbf{y}_2,\theta)ds\, d\mathbf{r}_0\, d\mathbf{y}_2\, d\theta. \tag{4.9}$$

The closure approximation and (4.9) allow us to solve for the constants of integration in (4.2b): $\mathbb{I}(1/2) = \bar{\mathbf{f}}_{\mathrm{m},2}/2$ and $\int\mathbb{I}(z)dz = \bar{\mathbf{f}}_{m,2}/6$. Plugging these expressions into (4.2b) yields the final gap-averaged fluid equations

$$\nabla_{x,2}\cdot\bar{\mathbf{u}}_2(\mathbf{x}_2) = 0, \tag{4.10a}$$

$$\bar{\mathbf{u}}_2(\mathbf{x}_2) = -\frac{A_0}{12}\nabla_2 q(\mathbf{x}_2) + \frac{B_0}{12}\bar{\mathbf{f}}_m(\mathbf{x}_2,t). \tag{4.10b}$$

This concludes the model reduction to a system of equations depending on the two-dimensional configuration variables $\mathbf{r}_0, \mathbf{x}_2$ and one-dimensional configuration variables s, θ. Table 2 summarizes the two-dimensional model equations. For simplicity, we drop the subscript 2 and bars in the notation and let $D_{\mathrm{t},||} = D_{\mathrm{t},||}^0 T^0/L^2$ and $D_{\mathrm{r}} = D_{\mathrm{r}}^0 T$.

5. Numerical method. In this section, we discuss the discretization of the nondimensionalized equations summarized in Table 2 and the development of a stable algorithm. First, we note that $\mathcal{M}_{\mathrm{b}}$ is high dimensional, with six variables in two

TABLE 2

Summary of the two-dimensional, gap-averaged, nondimensional model equations for the evolution of the filament distribution $\Psi(\mathbf{x},\theta,t)$, bound motor distribution $\mathcal{M}_b(\mathbf{r}_0,s|\mathbf{x},\theta;t)$, free motor distribution $\mathcal{M}_f(\mathbf{r}_0)$, and fluid $\mathbf{u}(\mathbf{x})$ in a motility assay.

Model equations		
Filaments	$\partial_t\Psi + \nabla_x\cdot(\dot{\mathbf{x}}\Psi) + \partial_\theta(\dot\theta\Psi) = 0$	(F1)
	$\dot{\mathbf{x}} = \mathbf{u} - D_{\mathrm{t},\|\|}\nabla_x \ln\Psi, \quad \dot\theta = \mathbf{p}_\perp^T\nabla_x\mathbf{u}\mathbf{p} - D_\mathrm{r}\partial_\theta\ln\Psi$	(F2)
Motors	$\partial_{t^*}\mathcal{M}_\mathrm{b} + \frac{1}{2}\partial_\mathrm{s}\mathcal{M}_\mathrm{b} = \frac{k_\mathrm{on}}{\iint_B \Psi d\mathbf{x}_2 d\theta}\mathcal{M}_\mathrm{f}\mathbb{1}_B - k_\mathrm{off}\mathcal{M}_\mathrm{b}$	(M1)
	$\mathcal{M}_\mathrm{f} = \mathcal{M} - \iiint \mathcal{M}_\mathrm{b}\Psi ds\, d\mathbf{y}\, d\theta$	(M2)
Fluid	$\mathbf{u} = -\frac{A_0}{12}\nabla_2 q + \frac{B_0}{12}\mathbf{f}_m, \quad \nabla\cdot\mathbf{u} = \mathbf{0}$	(U1)
	$\mathbf{f}_\mathrm{m} = -\frac{1}{2}\iiint \mathbf{p}\,\delta(\mathbf{y} + \frac{l}{L}s\mathbf{p} - \mathbf{x})\Psi\mathcal{M}_\mathrm{b} ds\, d\mathbf{r}_0\, d\mathbf{y}\, d\theta$	(U2)

dimensions. However, since a head detaches if the elongation of the motor's stalk exceeds a certain threshold, $\mathcal{M}_\mathrm{b}$ is sparse in the $\mathbf{x}-\mathbf{r}_0$ hyperplane; hence we store a small $\mathbf{x}_2$-grid, whose size depends on (l/L), around each $\mathbf{r}_0$.

At $t=0$, we initialize the filament distribution Ψ, the motor distribution $\mathcal{M}$, and the bound motor distribution $\mathcal{M}_\mathrm{b}$. The free motor distribution can then be computed with (M2) and the fluid equations (U1)–(U2) solved (see below). The algorithm steps and substeps to advance from time t^n to time t^{n+1} are described next. Since $\tau < T$, we denote by k the time index on which $\mathcal{M}_\mathrm{b}$ is solved.

1. Compute Ψ^{n+1} by solving (F1) together with (F2). We use second order Crank–Nicolson for the diffusion terms, and Adams–Bashforth 2 with an adaptive timestep for the time discretization of the advection terms. The advection terms are discretized in space using a high-resolution total variation diminishing upwind scheme with superbee flux limiter [7].
2. Compute $\mathcal{M}_\mathrm{b}^{k+1}$ by evaluating (M2) and solving (M1). The integrals in (M2) are evaluated using the midpoint rule using data at time n. We again use upwinding with superbee flux limiter for the advection terms, and Adams–Bashforth 2 with an adaptive timestep for the time discretization. We repeat this process until $\mathcal{M}_\mathrm{b}^{n+1}$ is obtained.
3. Compute the force density $\mathbf{f}_\mathrm{m}^{n+1}$ from (U2) using $\mathcal{M}_\mathrm{b}^{n+1}$ and Ψ^{n+1}. The integrals are evaluated using the midpoint rule and an approximate Dirac delta function, for which we use a hat function spanning two grid cells in each direction. This approximation is C_0 and satisfies a first moment condition, resulting in conservation of angular momentum. For a discussion of the implications of different choices of numerical delta functions, see [32].
4. Solve (U1) spectrally for $\mathbf{u}^{n+1}$. Because of the periodic boundary conditions, we transform (U1) in Fourier space ($\mathbf{k}$ wave vector):

$$\hat{\mathbf{u}}_\mathbf{k} = -\frac{A_0}{12}i\mathbf{k}\hat{p} + \frac{B_0}{12}\hat{\mathbf{f}}_{\mathrm{m}_\mathbf{k}}, \quad \mathbf{k}\cdot\hat{\mathbf{u}}_\mathbf{k} = 0.$$

Taking the dot product with $\mathbf{k}$, the pressure can be eliminated, yielding

$$\begin{cases} \hat{\mathbf{u}}_\mathbf{k} = \frac{B_0}{12}\left(\mathbf{I} - \frac{\mathbf{k}\mathbf{k}^T}{k^2}\right)\hat{\mathbf{f}}_{\mathrm{m}_\mathbf{k}} \text{ if } k = \|\mathbf{k}\| \neq 0, \\ \hat{\mathbf{u}}_\mathbf{0} = \frac{B_0}{12}\hat{\mathbf{f}}_{m_\mathbf{0}} \text{ if } k = 0. \end{cases} \tag{5.1}$$

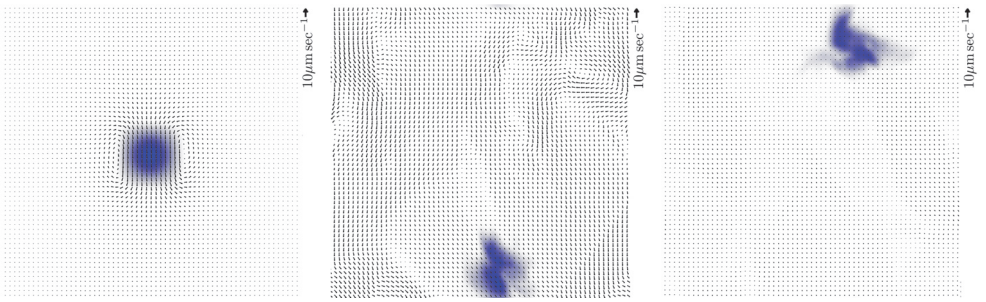

FIG. 2. *Evolution of the velocity field and filament density for a clump of locally aligned filaments with uniform bound motor density, depicted at* $t = 0$s, $t = 50$s, *and* $t = 150$s. *The parameters are* $L = 125\mu$m, $l = 1\mu$m, $\varepsilon = 5 \cdot 10^{-4}$, $N = 2 \cdot 10^4$, $N_m = 3 \cdot 10^6$, $k_{\text{on}} = 0.5\text{s}^{-1}$, $k_{\text{off}} = 0.5\text{s}^{-1}$. *The dimensionless diffusion parameters are* $D_{\text{t},||} = 2.5 \cdot 10^{-3}$ *and* $D_{\text{r}} = 2.5 \cdot 10^{-5}$.

We remark that the constants A_0 and Q_0 drop out and (5.1) depends on B_0 only. At this stage, we also compute the rate-of-strain tensor spectrally.

The two most time-intensive portions of the algorithm are the bound motor density evolution and the motor force calculation. For feasibility, we implemented these using Nvidia's CUDA C language and ran them on Nvidia Tesla GPU accelerators obtaining speedup factors of nearly 50 for all parameters tested. Since there is no interaction between motors in neighboring $\mathbf{r}_o$ cells, we update each $\mathbf{r}_0$ cell independently.

6. Results. We illustrate the behavior of the system with two examples, using the parameters $L = 125\mu$m, $l = 1\mu$m, $\varepsilon = 5 \cdot 10^{-4}$, $N = 2 \cdot 10^4$, $N_{\text{m}} = 3 \cdot 10^6$, $k_{\text{on}} = 1\text{s}^{-1}$, $k_{\text{off}} = 0.5\text{s}^{-1}$. Here we demonstrate that the proposed model captures qualitative features of microtubule gliding assays.

First we consider a clump of locally aligned filaments in the center of the domain with an initially uniform bound motor density. The initial alignment drives the fluid motion, and consequently the filaments, in that direction. The clump advects and diffuses through the domain as illustrated in Figure 2 (see supplementary movie S1). This motion is qualitatively similar to the moving clusters observed in [38]. The resulting disturbance in the velocity field propagates out from the leading edge of the clump in a wave-like motion. Eventually, diffusion causes the filament density to relax to the uniform isotropic density and the velocity field to decay to zero. We set the dimensionless diffusion parameters to $D_{\text{t},||} = 2.5 \cdot 10^{-3}$ and $D_{\text{r}} = 2.5 \cdot 10^{-5}$.

Second, we consider the experimentally motivated example of a gliding assay of nonlocalized filaments and motors (see Figure 3 and supplementary movies S2–S6). If the initial density of filaments is uniform, our model does not generate disturbance flows different from the imposed mean flow. Therefore, the filament density is perturbed away from uniformity in both space and orientation with

$$\frac{1}{a} \sum_{i,j=1}^{8} \epsilon_{ij} \cos(\pi i x + \xi_{ij}) \cos(\pi j y + \xi_{ij}) P_{ij}(\theta), \tag{6.1}$$

where ϵ_{ij} is a uniform random number in $[-.01, .01]$, ξ_{ij} is a uniform random number in $[0, 2\pi]$, a is a normalization constant, and $P_{ij}(\theta)$ are third order polynomials in $\cos(\theta)$ and $\sin(\theta)$ with random coefficients in $[-1, 1]$, as in [35].

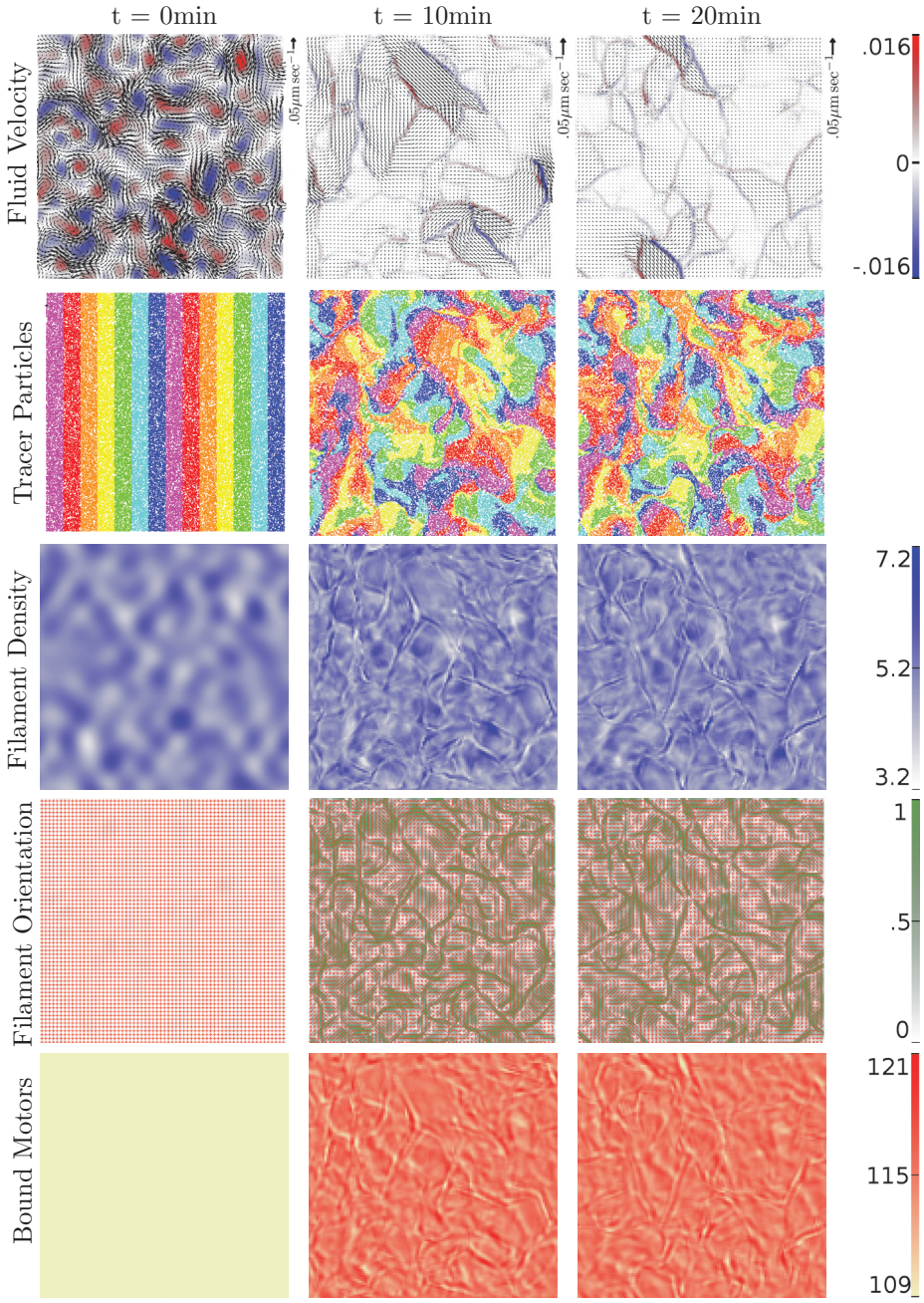

FIG. 3. *Emergence of ordered subregions in the filament-motor-fluid system, depicted at* $t = 0$ *(first column),* $t = 10\,\mathrm{min}$ *(second column), and* $t = 20\,\mathrm{min}$ *(third column). First row:* $\mathbf{u}(\mathbf{x}, t)$*, with vorticity plotted in color (online) (units of* s^{-1}*). As the simulation proceeds, the fluid subregions form vorticity bands at their boundaries with zero vorticity in their interiors. Second row: Tracer particles show fluid mixing. Third row:* $\Psi_{spatial}(\mathbf{x}, t)$ *in* μm^{-2} *defined in* (6.2)*. Fourth row: Eigenvectors of* $\mathbf{N}(\mathbf{x}, t)$ *(red lines, online) and* $S(\mathbf{x}, t)$ *(green field, online) given in* (6.3)–(6.4)*. Fifth row:* $\mathcal{M}_b^{tail}(\mathbf{r}_0, t)$ *in* μm^{-2} *defined in* (6.5)*. At* $t = 0$*, the density of filaments is perturbed in space and orientation according to* (6.1)*, while the bound motor density is uniform. The parameters are* $L = 125\mu\mathrm{m}$*,* $l = 1\mu\mathrm{m}$*,* $\mu = 0.12\mathrm{pNs}/\mu\mathrm{m}^2$*,* $\varepsilon = 5 \cdot 10^{-4}$*,* $N = 2 \cdot 10^4$*,* $N_m = 3 \cdot 10^6$*,* $k_{on} = 1\mathrm{s}^{-1}$*,* $k_{off} = 0.5\mathrm{s}^{-1}$*,* $D_{\mathrm{t},||} = 0\mu\mathrm{m}^2\mathrm{s}^{-1}$*,* $D_{\mathrm{r}} = 0\mathrm{s}^{-1}$*.*

The typical state of the system is illustrated in Figure 3 at times $t = 0, 10, 20$ min. The first row depicts the evolution of the velocity and vorticity fields (supplementary movie S2), and in the second row, tracer particles highlight fluid mixing (supplementary movie S3). After the transient velocity field disappears, the flow organizes into distinct subregions separated by boundaries of nonzero vorticity. These subregions span tens of microns, compared with the filament length of 1 micron, and can persist for several minutes. The third row shows the spatial filament density defined as

$$\Psi_{\text{spatial}}(\mathbf{x}, t) = \int \Psi(\mathbf{x}, \theta, t) d\theta \tag{6.2}$$

(supplementary movie S4). As t increases, the filaments form varying patterns, concentrating into bands at flow subregion boundaries and clumps in flow subregion interiors. These filament concentration patterns largely maintain their structure as they traverse the domain following the flow field. Some regions collide, resulting in the formation of larger fronts or bands, while others break apart. The concentrated regions contain more than twice as many filaments as the sparse regions. Such migrating cohesive structures have been observed in experiment [38, 39]. The fourth row depicts the filament orientation field (supplementary movie S5). We compute the orientation matrix

$$\mathbf{N}(\mathbf{x}, t) = \frac{\int \mathbf{p}\mathbf{p}^T \Psi(\mathbf{x}, \theta, t) d\theta}{\int \Psi(\mathbf{x}, \theta, t) d\theta} \tag{6.3}$$

and draw its eigenvectors scaled by their associated eigenvalues. We remark that Ψ maintains antipodal symmetry, i.e., $\Psi(\mathbf{x}, \theta, t) = \Psi(\mathbf{x}, \theta + \pi, t)$, because (4.6a)–(4.6b) are invariant under this transformation. The two-dimensional nematic order parameter is

$$S(\mathbf{x}, t) = \frac{\int \left(2(\mathbf{p} \cdot \mathbf{n})^2 - 1\right) \Psi(\mathbf{x}, \theta, t) d\theta}{\int \Psi(\mathbf{x}, \theta, t) d\theta}, \tag{6.4}$$

where $\mathbf{n}$ is the eigenvector associated with the largest eigenvalue of $\mathbf{N}$. We observe increased local nematic order at the boundaries of the flow subregions, where filaments tend to align tangentially to the boundaries, while the interiors of the flow subregions contain areas of both high and low nematic order. Finally, the fifth row depicts the bound motor concentration with tail at $\mathbf{r}_0$:

$$\mathcal{M}_{\text{b}}^{\text{tail}}(\mathbf{r}_0, t) = \iiint \mathcal{M}_{\text{b}}(s, \mathbf{r}_0, t | \mathbf{x}, \theta) \Psi(\mathbf{x}, \theta, t) ds d\mathbf{x} d\theta \tag{6.5}$$

(supplementary movie S6). Our simulation shows a strong positive correlation between high bound motor density and high filament concentration. We note that motors are not directly advected by the flow, as their tails are fixed to the substrate. Instead, the bound motor concentration increases as more filaments become available to bind to.

7. Conclusions. Starting from conservation equations, we developed a multiscale model describing the complex interplay between molecular motors, filaments, and fluid in a gliding assay. Our asymptotic and dimensional analysis agrees with experimental results [38] and shows that, for a small channel height, the filaments evolve in a two-dimensional plane parallel to the bottom plate upon which molecular motors

are anchored. The coupling between the motors, filaments, and surrounding fluid is achieved by directly spreading the motor force onto the fluid and passively advecting the filaments with the local fluid velocity. As a result, the depth-averaged fluid equations resemble the non-Newtonian Hele-Shaw equations. In the present model, we consider only a dilute suspension of filaments and therefore neglect effects due to steric interactions between filaments. The only interactions considered are therefore purely hydrodynamic interactions between the fluid and the filaments. Nevertheless, our simulations show behavior that is qualitatively similar to that seen in [38]. We observe swirls, moving high-density fronts, and cluster movements.

An in-depth study of the parameter set should reveal the transition between different states as described in [21, 17, 36]. While our model and numerical experiments demonstrate the importance of hydrodynamic interactions, they do not address the relative importance of steric and hydrodynamic interactions for pattern formation in gliding assays. To be able to ascertain the role of both effects as well as observe additional patterns, the density of filaments must be increased. As a result, the continuum model should be extended to include both steric interactions between the filaments and $\boldsymbol{\sigma}_F^{\mathrm{p}}$, the extra stress due to the filament resistance to deformation [9, 6].

REFERENCES

[1] G. K. Batchelor, *Slender-body theory for particles of arbitrary cross-section in Stokes flow*, J. Fluid Mech., 44 (1970), pp. 419–440.

[2] G. K. Batchelor, *The stress system in a suspension of force-free particles*, J. Fluid Mech., 41 (1970), pp. 545–570.

[3] R. B. Bird, C. F. Curtiss, R. C. Armstrong, and O. Hassager, *Dynamics of Polymeric Liquids, Volume* 2: *Kinetic Theory*, 2nd ed., Wiley-Interscience, New York, 1987.

[4] C. P. Brangwynne, F. C. MacKintosh, and D. A. Weitz, *Force fluctuations and polymerization dynamics of intracellular microtubules*, Proc. Natl. Acad. Sci. USA, 104 (2007), pp. 16128–16133.

[5] D. L. Coy, M. Wagenbach, and J. Howard, *Kinesin takes one* 8*-nm step for each ATP that it hydrolyzes*, J. Biol. Chem., 274 (1999), pp. 3667–3671.

[6] M. Doi and S. F. Edwards, *The Theory of Polymer Dynamics*, Oxford University Press, Oxford, UK, 1986.

[7] C. P. Dullemond, *Lecture on Numerical Fluid Dynamics*, University of Heidelberg, Heidelberg, Germany, http://www.mpia-hd.mpg.de/~dullemon/lectures/fluiddynamics08 (Summer 2008).

[8] S. A. Endow and D. S. Barker, *Processive and nonprocessive models of kinesin movement*, Annu. Rev. Physiol., 65 (2003), pp. 161–175.

[9] B. Ezhilan, M. J. Shelley, and D. Saintillan, *Instabilities and nonlinear dynamics of concentrated active suspensions*, Phys. Fluids, 25 (2013), 070607.

[10] T. L. Fallesen, J. C. Macosko, and G. Holzwarth, *Force-velocity relationship for multiple kinesin motors pulling a magnetic bead*, Eur. Biophys. J., 40 (2011), pp. 1071–1079.

[11] L. Giomi, L. Mahadevan, B. Chakraborty, and M. F. Hagan, *Excitable patterns in active nematics*, Phys. Rev. Lett., 106 (2011), 218101.

[12] W. O. Hancock and J. Howard, *Kinesin's processivity results from mechanical and chemical coordination between the ATP hydrolysis cycles of the two motor domains*, Proc. Natl. Acad. Sci. USA, 96 (1999), pp. 13147–13152.

[13] J. Howard, *The movement of kinesin along microtubules*, Annu. Rev. Physiol., 58 (1996), pp. 703–729.

[14] J. Howard, *Mechanics of Motor Proteins and the Cytoskeleton*, Sinauer Associates, Sunderland, MA, 2001.

[15] J. Howard, A. J. Hudspeth, and R. D. Vale, *Movement of microtubules by single kinesin molecules*, Nature, 342 (1989), pp. 154–158.

[16] E. Karsenti, F. J. Nédélec, and T. Surrey, *Modelling microtubule patterns*, Nat. Cell Biol., 8 (2006), pp. 1204–1211.

[17] J. Kierfeld, K. Frentzel, P. Kraikivski, and R. Lipowsky, *Active dynamics of filaments in motility assays*, Eur. Phys. J. Special Topics, 157 (2008), pp. 123–133.

[18] S. Klumpp and R. Lipowsky, *Cooperative cargo transport by several molecular motors*, Proc. Natl. Acad. Sci. USA, 102 (2005), pp. 17284–17289.
[19] L. Kondic, P. Palffy-Muhoray, and M. J. Shelley, *Models of non-Newtonian Hele-Shaw flow*, Phys. Rev. E, 54 (1996), pp. R4536–R4539.
[20] C. B. Korn, S. Klumpp, R. Lipowsky, and U. S. Schwarz, *Stochastic simulations of cargo transport by processive molecular motors*, J. Chem. Phys., 131 (2009), 245107.
[21] P. Kraikivski, R. Lipowsky, and J. Kierfeld, *Enhanced ordering of interacting filaments by molecular motors*, Phys. Rev. Lett., 96 (2006), 258103.
[22] K. Kruse, J.-F. Joanny, F. Jülicher, J. Prost, and K. Sekimoto, *Asters, vortices, and rotating spirals in active gels of polar filaments*, Phys. Rev. Lett., 92 (2004), 078101.
[23] K. Kruse, J.-F. Joanny, F. Jülicher, J. Prost, and K. Sekimoto, *Generic theory of active polar gels: A paradigm for cytoskeletal dynamics*, Eur. Phys. J. E, 16 (2005), pp. 5–16.
[24] H. Y. Lee and M. Kardar, *Macroscopic equations for pattern formation in mixtures of microtubules and molecular motors*, Phys. Rev. E, 64 (2001), 056113.
[25] T. B. Liverpool and M. C. Marchetti, *Bridging the microscopic and the hydrodynamic in active filament solutions*, Europhys. Lett., 69 (2005), pp. 846–852.
[26] S. A. McKinley, A. Athreya, J. Fricks, and P. R. Kramer, *Asymptotic analysis of microtubule-based transport by multiple identical molecular motors*, J. Theoret. Biol., 305 (2012), pp. 54–69.
[27] D. Mizuno, C. Tardin, C. F. Schmidt, and F. C. MacKintosh, *Nonequilibrium mechanics of active cytoskeletal networks*, Science, 315 (2007), pp. 370–373.
[28] F. Nédélec, *Computer simulations reveal motor properties generating stable antiparallel microtubule interactions*, J. Cell Biol., 158 (2002), pp. 1005–1015.
[29] F. Nédélec and D. Foethke, *Collective Langevin dynamics of flexible cytoskeletal fibers*, New J. Phys., 9 (2007), 427.
[30] F. J. Nédélec and T. Surrey, *Dynamics of microtubule aster formation by motor complexes*, C. R. Acad. Sci. Paris, 2 (2001), pp. 841–847.
[31] F. J. Nédélec, T. Surrey, A. C. Maggs, and S. Leibler, *Self-organization of microtubules and motors*, Nature, 389 (1997), pp. 305–308.
[32] C. Peskin, *The immersed boundary method*, Acta Numer., 11 (2003), pp. 479–517.
[33] S. L. Rogers and J. M. Scholey, *Motility assays for microtubule motor proteins*, in eLS, John Wiley & Sons, Chichester, UK, http://www.els.net/WileyCDA/ElsArticle/refId-a0002621.html (March 2004).
[34] D. Saintillan and M. J. Shelley, *Instabilities and pattern formation in active particle suspensions: Kinetic theory and continuum simulations*, Phys. Rev. Lett., 100 (2008), 178103.
[35] D. Saintillan and M. J. Shelley, *Instabilities, pattern formation, and mixing in active suspensions*, Phys. Fluids, 20 (2008), 123304.
[36] S. Sankararaman, G. I. Menon, and P. B. SunilKumar, *Modelling pattern formation in motor-microtubule mixtures*, Phys. Scripta, T106 (2003), pp. 26–31.
[37] S. Sankararaman, G. I. Menon, and P. B. SunilKumar, *Self-organized pattern formation in motor-microtubule mixtures*, Phys. Rev. E, 70 (2004), 031905.
[38] V. Schaller, C. Weber, C. Semmrich, W. Frey, and A. R. Bausch, *Polar patterns of driven filaments*, Nature, 467 (2010), pp. 73–77.
[39] Y. Sumino, K. H. Nagai, Y. Shitaka, D. Tanaka, K. Yoshikawa, H. Chate, and K. Oiwa, *Large-scale vortex lattice emerging from collectively moving microtubules*, Nature, 483 (2012), pp. 448–452.
[40] T. Surrey, F. J. Nédélec, S. Leibler, and E. Karsenti, *Physical properties determining self-organization of motors and microtubules*, Science, 292 (2001), pp. 1167–1171.
[41] S. Swaminathan, F. Ziebert, D. Karpeev, and I. S. Aranson, *Motor-mediated alignment of microtubules in semidilute mixtures*, Phys. Rev. E, 79 (2009), 036207.